

Stateful characterization of resistive switching TiO₂ with electron beam induced currents

Running title: Stateful EBIC

Running Authors: Hoskins, *et al.*

Brian D. Hoskins^{1,2,a}, Gina C. Adam^{3,4}, Evgheni Strelcov^{1,5}, Nikolai Zhitenev¹,
Andrei Kolmakov¹, Dmitri B. Strukov³, Jabez J. McClelland¹

¹)Center for Nanoscale Science and Technology, National Institute of Standards and Technology, Gaithersburg, MD 20852, USA

²)Materials Department, University of California Santa Barbara, Santa Barbara, CA 93106, USA

³)Electrical and Computer Engineering Department, University of California Santa Barbara, Santa Barbara, CA 93106, USA

⁴)Institute for Research and Development in Microtechnologies, 077190 Bucharest, Romania

⁵)Maryland NanoCenter, University of Maryland, College Park, MD 20742, USA

^a) Electronic mail: brian.hoskins@nist.gov

Metal oxide resistive switches have become increasingly important as possible artificial synapses in next generation neuromorphic networks. Nevertheless, there is still no codified set of tools for studying fundamental properties of the devices. To this end, we demonstrate electron beam induced current (EBIC) measurements as a powerful method to monitor the development of local resistive switching in TiO₂ based devices at the nanoscale. By comparing beam-energy dependent EBIC with Monte Carlo simulations of the energy absorption in different layers of the device, it is possible to deconstruct the origins of switching filament image formation and relate this directly to both morphological changes and the state of the switch. By clarifying the contrast mechanisms in EBIC it is possible to gain new insights into the scaling of the resistive switching phenomenon and observe the formation of an excessive current leakage region around the switching filament. In addition, analysis of symmetric device structures reveals the presence of propagating polarization domains.

I. INTRODUCTION

Metal oxide resistive switches (memristors) have been of intense interest for use in next generation memory or as analog weights in neuromorphic networks. Their unique properties, including 2-terminal structure, scalability (>10 nm), nonvolatility (>10 years at 85 °C), high endurance (>10¹² cycles), and low energy consumption (<10 pJ), are ideal

for next generation hardware[1-3]. However, the complex nature of the switching in these devices, speculated to involve coupling of chemical, electrical, and thermal fields, has stymied a comprehensive understanding of the process[4].

A metal oxide resistive switch consists of two metallic layers separated by a substoichiometric oxide and acts as a programmable resistor. While the switching process is not fully understood, it is generally believed to involve the motion of oxygen vacancies in the oxide under electrical fields and thermal gradients[5-7]. This ion motion leads to a local, nanometer-scale variation in the vacancy concentration and a corresponding variation in the thickness of the oxide's depletion region. The vacancy concentration often appears to grow like a metallic nanoscale filament, and as the depletion region thickness declines, the conductance passes from being controlled by thermionic, to thermionic field, and ultimately to field emission.

Several studies have been conducted probing the underlying physics of the switching and explore the origin and dynamics of filament formation in resistive switches. However, work so far has not yielded a comprehensive picture. Transmission electron microscopy studies suggest that the underlying structural changes during switching can be small, particularly under conditions where the switching is controlled by current compliance[9]. Investigations using scanning transmission x-ray microscopy have probed the chemical changes in devices through the forming process, but have not managed to view single cycle changes or correlate observed large area chemical changes with local changes in the conductivity[10, 11]. The chemical variations between conductive and insulating configurations are highly localized and are therefore hard to quantify with available spectroscopic tools, particularly in the presence of a large

deformation region[12]. Measurements with scalpel scanning probe microscopy (SPM) have provided precise measurements of filament behavior. However, the destructive nature of this technique makes it difficult to explore the full parameter space, since it only analyzes a single switching event[13].

In the present work, we employ high resolution scanning electron microscopy (SEM)-based electron beam induced current microscopy (EBIC) to systematically explore switching in TiO₂ devices. We present detailed imaging of filament formation as a function of resistive state, and also explore the physical mechanisms of current generation. EBIC has been used previously to characterize resistive switching devices, but the relatively low resolution ($\approx 1 \mu\text{m}$) and the absence of a fundamental understanding as to the mechanisms of image formation – due to a lack of stateful and energy dependent data – has so far made it impossible to draw conclusions as to the origin of the generated current and the nature of the filament and its surrounding deformation region[25, 26]. By exploring variations in the generated signal in different device geometries as a function of beam energy and resistive state, we show it is possible to probe the underlying physics of the resistive switching devices, clarify the image formation mechanisms, and develop a reliable means of observing filament formation and distinguishing it from non-filament areas. This approach to stateful characterization is robust to measurement artifacts by being selective to the reversible changes in the device.

In EBIC, few-electron-volt secondary electrons and electron-hole pairs created by a primary beam at 250 eV to 25 keV (Figure 1.a) interact strongly with the built-in device fields. Current is collected via auxiliary electrodes connected to different parts of

the device (Figure 1.b), resulting in a local measurement of the conductance stimulated by the incident electron beam [14].

The large number of interfaces in a metal-insulator-metal (MIM) structure such as a metal oxide resistive switch leads to competing currents that sum to the measured EBIC current (I_{EBIC}). We can write:

$$I_{EBIC} = I_{EBAC} + I_{SEE} + I_{e\leftrightarrow h} + I_{ISEE}^{T\rightarrow B} + I_{ISEE}^{B\rightarrow T}, \quad (\text{Eq. 1})$$

where I_{EBAC} is the current absorbed from the incident electron beam (incident current less any backscattered or transmitted current), I_{SEE} is the secondary electron emission current, $I_{e\leftrightarrow h}$ is the electron-hole-pair separation current, $I_{ISEE}^{T\rightarrow B}$ is the internal secondary electron current from the top electrode to the bottom electrode, and $I_{ISEE}^{B\rightarrow T}$ is the internal secondary electron current from the bottom electrode to the top electrode. Figure 2.a shows approximate locations of the sources of these currents and their polarities. I_{EBAC} and I_{SEE} are universal to all materials, since they represent the injected current and emitted electrons to vacuum. $I_{e\leftrightarrow h}$, produced when e-beam-induced electron-hole pairs are created at junctions between materials and separated by built-in fields, is often the largest and most commonly measured EBIC partition [15-17]. $I_{ISEE}^{T\rightarrow B}$ and $I_{ISEE}^{B\rightarrow T}$ are unique to MIM structures and result from thermionic emission, diffusion, or tunneling of hot electrons from one electrode to the other[18-20]. In a conventional MIM diode, the internal secondary electron currents are usually negligible, but become measurable at large applied biases (V_b) due to a lowering of the barrier height.

Each current can be a probe of the device behavior, e.g. indicating morphological changes such as crystallization or ripening. Since barrier lowering and raising *is resistive switching*, measurable quantities of $I_{ISEE}^{T\rightarrow B}$ and $I_{ISEE}^{B\rightarrow T}$ are observable in the absence of an

applied bias when the device is switched to the on-state, increasing the probability of hot electron transmission.

It can be difficult to deconvolve the sources of current in the device. However, a general principle of EBIC is that the observed current and electron yield (or nanoampere of signal per nanoampere of injected current), is proportional to the energy deposited into the specific layer sourcing the current. Since beam penetration and absorption primarily depend on the incident beam energy, the ratios of different current contributions will depend on the incident beam energy[21]. Variations in these ratios are predicted by simulating the energy absorbed in using Monte Carlo electron simulators[22-24]. Figure 2.a shows a 2-dimensional projection, and Figure 2.b. shows a depth profile, for these processes in a Pt/TiN/TiO_x/Pt structure for different energies. With increasing incident energy, the absorbed energy in the buried TiO_x starts small due to a lack of beam penetration, rises as the beam reaches the layer, and falls as the decreasing cross-section causes most of the energy to be transmitted. If there is a single built-in field across the layer the measured electron yield should be proportional to the absorbed energy.

II. EXPERIMENTAL

Three different kinds of metal oxide resistive switches (Figures 2.c) were constructed. Asymmetric structures were made in a standard form, Pt/TiO_x/TiN/Pt, and an inverted form, Pt/Ti/TiO_x/Pt, as well as a symmetric form Pt/TiO_x/Pt. Samples were mounted in a conventional Schottky-emission SEM with electrical feedthroughs connected to the device and a stage-mounted Faraday cup for calibrating the injected current. Measurements were done in cycles of grounding the device, programming the

device, grounding the device, connecting the current amplifier, and then imaging the device. The effect of changing the device conductance (as measured at 0.1 V) was probed by observing the EBIC signal at individual locations on the device as well as by summing the total signal within an image after subtracting the background due to the surrounding pristine area. Comparing the change in total integrated EBIC signal with respect to the off-state compactly quantifies changes in the state of the device.

We also used beam-induced defect formation to improve the reliability of the forming process[27, 28]. The dielectric breakdown needed to create switching could be initiated by the combined application of voltage and a large e-beam current at 5 keV. This electron beam assisted forming process made it possible to deterministically locate the breakdown region and consequently the filament (See Supplement Sec. V).

The image formation mechanisms were probed by imaging the same locations repeatedly with beam energies from 250 eV to 25 keV. Plotted ratios of injected current to EBIC current (the electron yield) were compared to layer-by-layer energy absorption plots predicted from Monte Carlo simulations of low energy electrons in the different device structures to determine the origins of different currents[24, 29].

III. RESULTS AND DISCUSSION

I. Virgin Device Measurements

In measurements of virgin asymmetric devices, the EBIC signal arises from an electron flow from low work function (TiN) to high work function contacts (Pt). Consequently, standard device structures exhibited negative absolute current, and inverted structures exhibited positive absolute current (Figure 3). Symmetric structures were observed to have a more complex behavior, occasionally exhibiting one polarity or

the other as well as significant relaxation and charging of the pad (See Supplement Sec. IV).

The energy dependence of the EBIC signal for the different device structures followed the Monte Carlo simulations of energy absorbed in the TiO_x , achieving maximum amplitude at 3.5 keV and 2 keV for the standard and inverted structures respectively (Figure 3b). For the standard structure (a top TiN layer) the signal polarity switches from positive to negative at energies above 1 keV, as the secondary electron emission into the vacuum (at low energy) is overcome by the background hole-pair signal (note that the secondary electron yield signal is not included in the Monte Carlo model)[30].

The internal quantum efficiency of the EBIC process can be estimated by combining the simulations with the Alig and Bloom relation[31, 32]:

$$E_i \approx 3E_g + 1 \text{ eV}, \quad (\text{Eq. 2})$$

where E_i (the effective pair creation energy) is substituted for E_g (the band gap) in calculations for collection efficiency, η , such that:

$$\eta \approx \frac{E_i}{E_{\text{absorbed}}} \frac{I_{\text{EBIC}}}{I_{\text{beam}}}, \quad (\text{Eq. 3})$$

where I_{EBIC} and I_{beam} are the measured EBIC and incident beam currents respectively[33]. For the standard structure at 5 keV, the simulation predicts that 50 electron-hole pairs per incident electron should be generated, as opposed to a measured 4, suggesting a collection efficiency of 8 %.

II. Switched device, asymmetric structure

Switched-on devices exhibited morphological changes, namely local electrode reconstruction (both minor and severe), as well as a relatively circular deformation region

(300 nm is diameter) which had an increase in the internal collection efficiency (Figure 4.d, 5 keV). In what follows, the signal discussed refers to the change in EBIC current relative to the current measured in virgin structures (the background current). Standard device structures, at low energy, exhibited a positive polarity signal within the deformation region when the device was in the on state (Figure 4.d, 1 keV). This positive signal correlated with the state of the device, and vanished when the device was programmed into the off state – indicating the signal is associated with the filament. Measurements as a function of energy showed that the signal achieves a maximum at 1.5 keV, a value consistent with top electrode absorption (Figure 4.a). The polarity and beam energy of the signal maximum suggests that the EBIC signal is due to internal secondary electron emission (ISEE). This is further supported by determining whether the polarity of the filament signal remains unchanged in the inverted devices. Since beam-electrode collisions generate hot electrons, the signal current polarity should be independent of the filament orientation, and, indeed, inverting the device did not cause a reversal in the polarity of the signal (See Supplement Sec. VI).

Tracking the ISEE signal across a region provides a qualitative measure of barrier height and also the extent of hot-electron conduction. Summing up the total differential current with respect to the off-state through a turn-on and turn-off event, it is apparent that the ISEE signal follows a power law with exponent < 1 as a function of conductance as the device is programmed into the off state (Figure 5.a), and scales nearly linearly with conductance as the device is programmed into the on-state (Figure 5.b). The different scaling relationships between the turn-on and turn-off branches suggest contrasting mechanisms for the filament formation and dissolution respectively.

In filaments, models of the conductance often use an Arrhenius relationship with exponent $\frac{\varphi_{eff}}{k_b T_o}$, where φ_{eff} is the effective thermal activation for conduction, k_b is Boltzmann's constant, and T_o is the ambient temperature. Competing modes of conduction often include Poole-Frenkel emission, space charge limited conduction, and interfacial resistance depending on the resistive state[8]. These models capture the most attractive feature of resistive switches, i.e., the ability to continuously tune their resistance by varying φ_{eff} between maximal (φ_{off}) and minimal (φ_{on}) values (Figure 1.e).

Consequently, one interpretation suggests that the on-branch switching is area dependent, driven by nucleation, saturation, and expansion of the filament, producing a signal proportional to the *area* (A), whereas the turn-off process is *barrier dependent* (through φ_{eff}), determined entirely by a local state variable (such as the oxygen vacancy concentration). Such a difference has been proposed in some thermophoresis based models of resistive switching[34, 35]. In drift-diffusion models it is potentially possible to explain based on the differing dopant profiles produced by drift/diffusion acting in concert or in opposition to one another, as well as by including 2-dimensional effects [34, 36].

The scaling relationships during the turn-on and turn-off branches can be analyzed assuming the zero-bias conductance σ follows the behavior of a Schottky junction,

$$\sigma = \left. \frac{dI_{Schottky}}{dV} \right|_{V=0} = \alpha A \exp\left(-\frac{\varphi_{eff}}{k_B T_o}\right), \quad (\text{Eq. 4})$$

where α is a prefactor, A is the area of the filament, φ_{eff} is the effective barrier height, and T_0 is the ambient temperature[37]. The ISEE can be assumed to follow thermionic emission theory, with a characteristic hot electron temperature, T_e , such that[18, 19]

$$I_{ISEE} = \beta A e \frac{\varphi_{eff}}{k_B T_e}. \quad (\text{Eq. 5})$$

Assuming the barrier height is constant, as might occur if nucleation and growth dominates in the turn-on branch, the two values will be proportional to one another. If, however, the effective barrier height varies due to barrier lowering, then the relationship between I_{ISEE} and σ will vary by:

$$I_{ISEE} = \frac{A\beta}{(A\alpha)^{T_e}} \frac{T_0}{T_e} \sigma^{T_e}, \quad (\text{Eq. 6})$$

where $\frac{T_0}{T_e}$ is the scaling parameter relating the ISEE current to the conductivity. Since the hot electron temperature is greater than ambient, $\frac{T_0}{T_e}$ should be strictly less than unity. The extracted value of 0.44 is consistent with this, suggesting an average hot electron temperature of 700 K. How extracted parameters like T_e vary will depend on the underlying model. Understanding the scaling between fit parameters and values extracted from other methods, such as the temperature coefficient of resistivity of the device, may help clarify these underlying mechanisms[38].

III. Imaging the effects of leakage currents around the filament

In the area surrounding the filament, we observed a deformation region, which acts as a non-programmable leakage path through which excess current can flow (Figure 6.d). Forward biasing the junction during turn-off leads to significant power dissipation, with a maximum occurring at -1.7 V and a leakage current of 2 mA (Figure 6.b). Device

cycling leads to secondary switching effects in the deformation region, and this was observed after a 10-cycle test (Figure 6.b). The SEM images before (Figure 6.a) and after (Figure 6.c) reveal increased secondary electron emission, caused by grain ripening, in the regions corresponding to the leakage[39]. This correlation of power dissipation with the deformation region, as opposed to being centered on the filament, suggests that managing damage induced by the filament formation is more important than controlling changes to the filament itself. Reducing the device size below the breadth of the deformation region is the simplest possible means of reducing the leakage. With the current density in this region running at $\approx 7.8 \cdot 10^{10}$ A/m² during the turn off process, a reduction to a 10 nm \times 10 nm structure would reduce the leakage to 6 μ A. Adding interfacial layers or otherwise engineering the device could also yield benefits by changing the specific contact resistance.

IV. Switched device symmetric structure

The questions of scaling and polarization take on new meaning in a symmetric device with dual Pt electrodes. In the asymmetric structures, overdriving the devices leads to electrode degradation and migration of the switching spot to a new location. Degradation is also present in symmetric structures, but coexists with domains of programmable polarization. This was observed by increasing the voltage stress and cycling the bias between negative and positive polarities, which led to increasing amplitude changes in the orientation of the built-in electric fields as measured by EBIC (Figures 7.a-d and 7.j).

A stepwise motion through the switching reversal (Figures 7.e-i) reveals a propagating domain wall. A measure of the total integrated signal through this transition

shows a maximum in the conductivity as the signal sum passes through zero, suggesting highest conductivity when the two polarizations are in balance, with a large domain wall between them (Figure 7.k). The theory of complementary resistive switching suggests that the conductivity will be highest at the interface between these two regions, and so the power dissipation and switching will be preferentially located here (Figures 7.h and 7.l) inducing its propagation[40-42]. We observed that some boundaries were less mobile than the primary one, which may be due to local variations in the grain orientation, crystallinity, or in the composition induced by the high stress.

The differences between the symmetric and asymmetric structures can be attributed to the competing scaling relationships that characterize them. As an asymmetric device is further polarized, its conductivity will only increase until some physical limit, like the temperature of melting, is reached. This is also true in the case of symmetric structures, but a sufficiently polarized device will ultimately decrease in conductivity due to field reversal. The reduction in dissipated power provides an opportunity for adjacent regions to also switch and likewise undergo inversion without the total power dissipation becoming large. This suggests that changes to the device structure, such as the asymmetry, specific resistance, or the heat dissipation change the scaling of the switching.

IV. SUMMARY AND CONCLUSIONS

We demonstrate energy dependent and stateful EBIC measurements on conventional resistive switching devices. Comparing these measurements to Monte Carlo simulations reveals two competing forms of contrast: classic excite-and-separate EBIC, and internal secondary electron emission (ISEE) which had not previously been distinguished. Stateful

measurements of the ISEE current showed different scaling relationships for the turn-on and turn-off branches which suggests the existence of different, hysteretic mechanisms for filament formation and dissolution. Symmetric device structures showed propagating fronts of different polarizations, depending on the direction of the applied bias prior to the image acquisition. This large area switching suggests that the details of device manufacture and geometry can have a significant effect on the underlying scaling of the resistive switching. These effects are difficult to observe spectroscopically, but become clear with EBIC.

Contributions

NZ, AK, DBS, BDH, and JJM conceived the experiment. BDH, GCA, and DBS designed the devices. BDH and GCA fabricated the devices. BDH, ES, AK, NZ and JJM developed experimental procedures and designed electronics. BDH performed the measurements and wrote the manuscript. All contributors discussed the experimental results and edited the manuscript.

Acknowledgements

We would like to thank Brian Thibeault and the UCSB nanofab staff for support in the device development. We would like to thank Alan Band, Glenn Holland, and David Rutter for their support in development of the experimental setup. We would like to thank Alexander Liddle for use of his microscope and useful discussions. We would like to thank Andrea Centrone for helpful discussions on the device structure. We would like to thank Mirko Prezioso on helpful discussions on the physics of the measurement. We would like to thank Jason E. Douglas for reviewing the manuscript. This work was supported by the AFOSR MURI grant FA9550-12-1-003 and NIST 70NANB 14H185. ES acknowledges support under the Cooperative Research Agreement between the University of Maryland and the National Institute of Standards and Technology Center for Nanoscale Science and Technology, Award 70NANB10H193, through the University of Maryland.

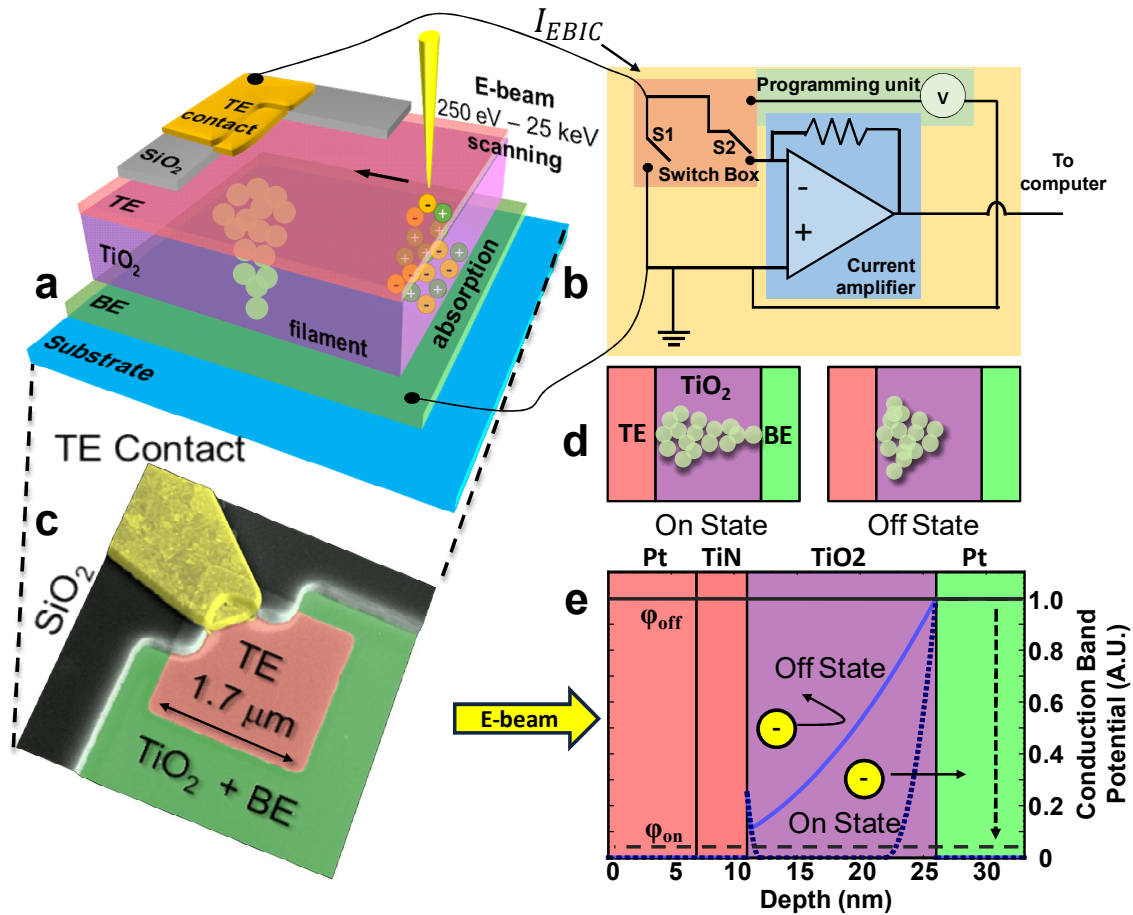


Figure 1. a) 3-D depiction of the experimental EBIC measurement including top electrode (TE), the TE contact, bottom electron (BE), e-beam with its generated carriers, dielectric layer (TiO_2), and the programmable filament. b) Basic electric measurement setup including switch box with grounding switch (S1) and exchange between imaging (with the current amplifier) and programming (S2). c) False color, 3-dimensional projected SEM image of the device including top electrode, bottom electrode, top contact, and SiO_2 . The incipient e-beam (250 eV to 25 keV) generates electron-hole pairs in the diode which are collected in an external ammeter. d) Simplified schematic depiction of the filament in the On State (spanning the Top Electrode (TE) to the Bottom Electrode (BE)) and the Off State (leaving an insulating barrier). e) Simplified depiction of the response of generated carriers to the built-in fields when experiencing a large effective barrier at the interface (ϕ_{off}) and a small effective barrier (ϕ_{on}).

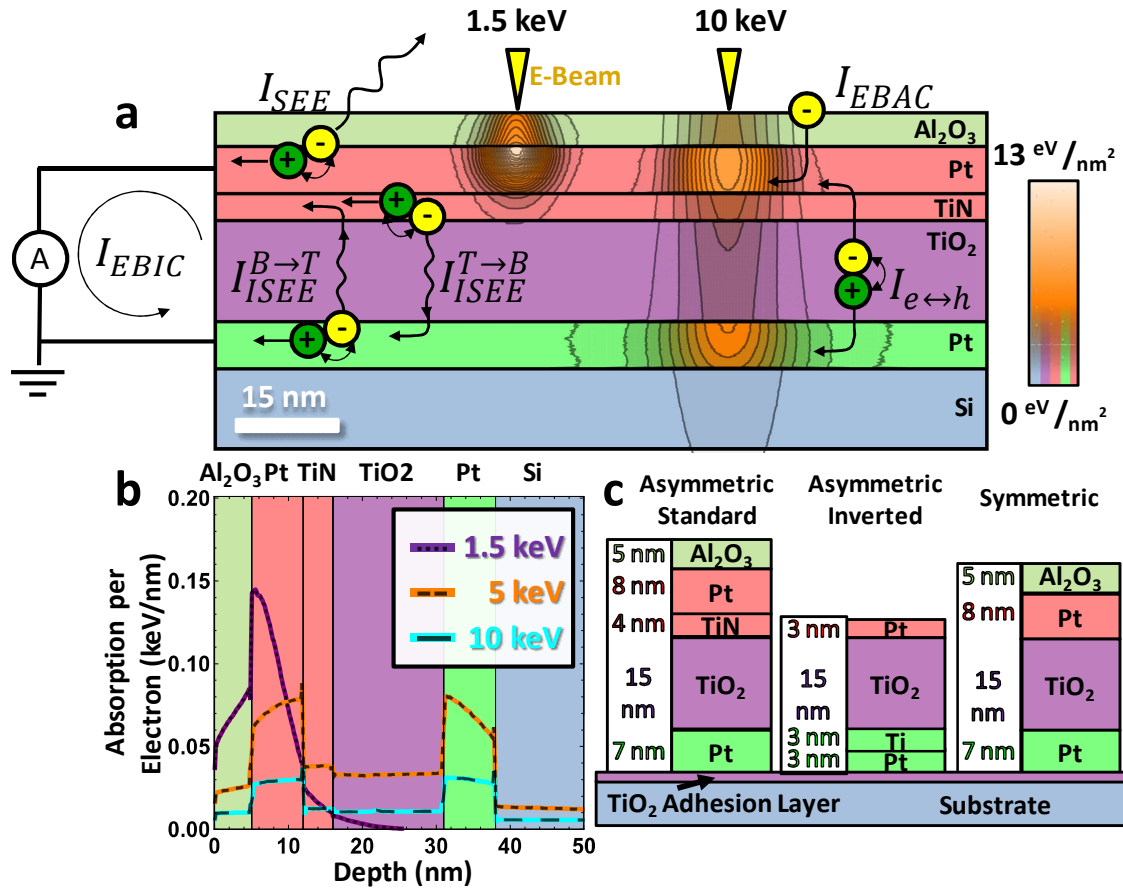


Figure 2. a) Monte Carlo simulated absorption in a multi-layer ReRAM device at both 1.5 keV incident beam and 10 keV incident beam. Absorption in different layers can result in the different depicted currents including the secondary electron current (I_{SEE}), the electron beam absorbed current (I_{EBAC}), the electron-hole pair current ($I_{e \leftrightarrow h}$), and the internal secondary electron currents from top-to-bottom ($I_{ISEE}^{T \rightarrow B}$) and bottom-to-top ($I_{ISEE}^{B \rightarrow T}$). These all sum to create the measured EBIC current (I_{EBIC}). b) Simulated 1-dimensional absorption profile in an ReRAM stack for different beam energies. Energy absorbed in the TiO_2 layer first rises and then falls with increasing beam energy. Note any energy absorbed in the silicon does not contribute to the measured EBIC current. c) Device stack of the different structures analyzed. The protective Aluminum oxide was stripped from the inverted device and the Pt made thinner in an attempt to increase the resolution.

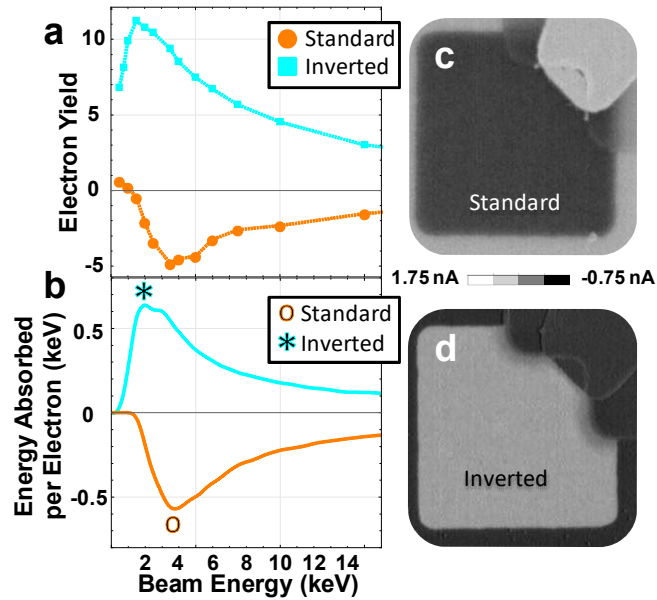


Figure 3. a) Measured energy dependence of the EBIC signal for the virgin device area in standard and inverted devices. The measured current is negative in standard device and positive in inverted device. The change in sign when flipping the device over is due to reversal of the built-in field. Error bars, reflecting single standard deviation of the mean, are smaller than the markers and are determined from an area of at least 50×50 pixel bounding box on each pad. b) Monte Carlo simulation results of inverted and standard structure absorbed energy per electron. Standard structure simulation result is shown with negative sign since absorbed energy is not a negative quantity and current direction is determined by structure. c) 5 keV EBIC image of a standard device. d) 2 keV EBIC image of an inverted device. The strong similarity between the measured and simulated curves show the strong relationship between absorbed energy and generated EBIC current.

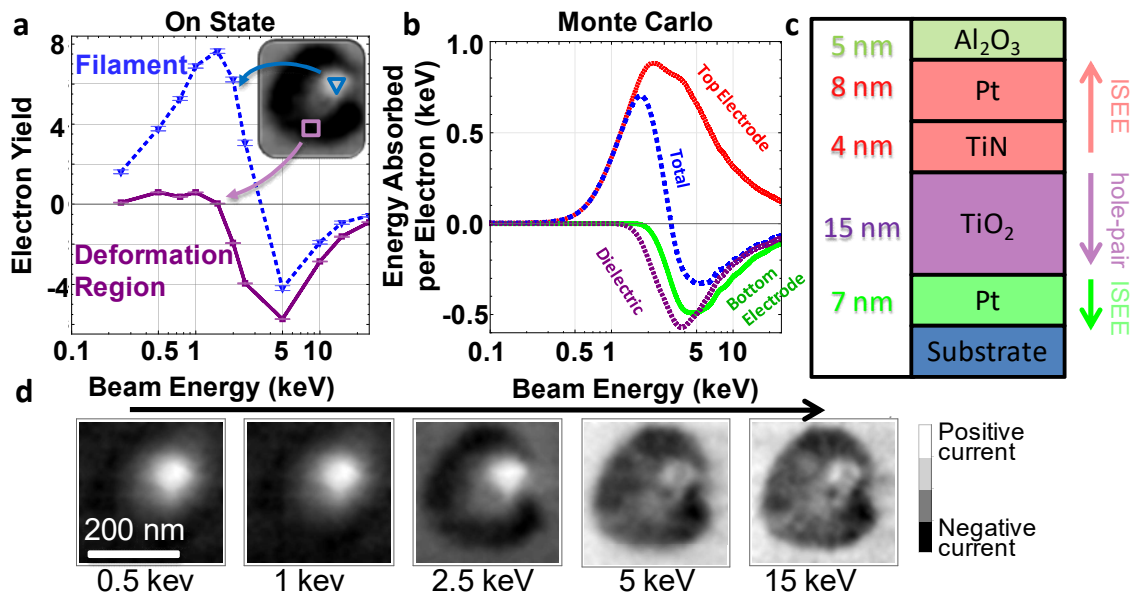


Figure 4. a) Measured electron yield as a function of energy. Error bars indicate single standard deviation of the mean within an 11×11 pixel bounding box at two indicated positions (inset). All quantities are

measured with respect to the background. b) Monte Carlo simulations on an asymmetric standard structure of absorption in each layer as a function of energy summarizing contributions from all elements of the structure. c) Device structure used in Monte Carlo Simulation with arrows indicating expected direction for ISEE and hole-pair separation currents. d) EBIC micrograph series showing contrast evolution with beam energy. Grey scale is qualitative for each image. The comparison of the measured currents to the simulated absorption profile makes it possible to determine the origins of the different EBIC currents.

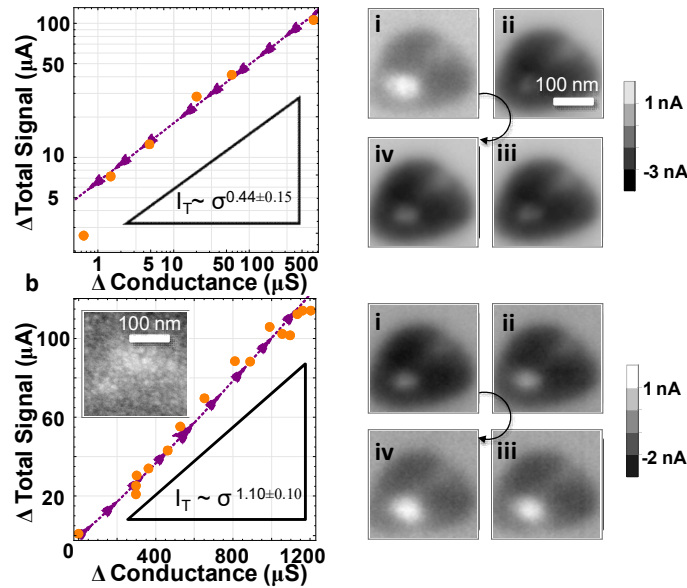


Figure 5. Comparison of the change in conductance measured at 0.1 V from the off state (Δ Conductance) and the measured change in total signal in an image (Δ Total Signal) a) (Left) Scaling dependence of total EBIC signal at 5 keV in turn-off branch with sublinear exponent 0.43 ± 0.15 (95 % confidence) and (i-iv) subset of 4 images taken during turn off. b) (Left) Scaling dependence of total EBIC signal in turn-on branch with near linear exponent 1.10 ± 0.10 (95 % confidence), (inset) SEM image after switching showing no degradation of the electrode, and (i-iv) subset of four 5 keV EBIC images taken during turn on. Scale bar is 100 nm for all images. Significant read disturb from filament-beam interaction on the turn on branch resulted in scatter in the data.

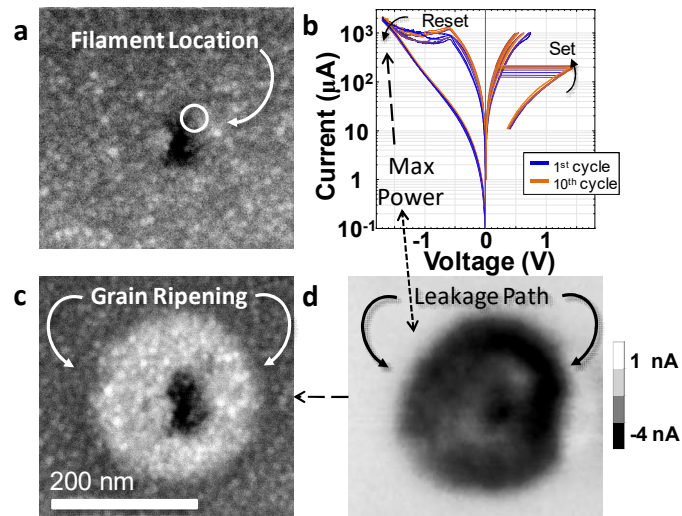


Figure 6. a) SEM micrograph of an asymmetric standard device after forming and switching twice. Area adjacent to the filament is damaged by the switching. b) depiction of 10 switching curves taken after image “a”. c) SEM micrograph and d) corresponding EBIC image showing correspondence between grain ripening (seen in c) and background deformation region (region of negative current in d).

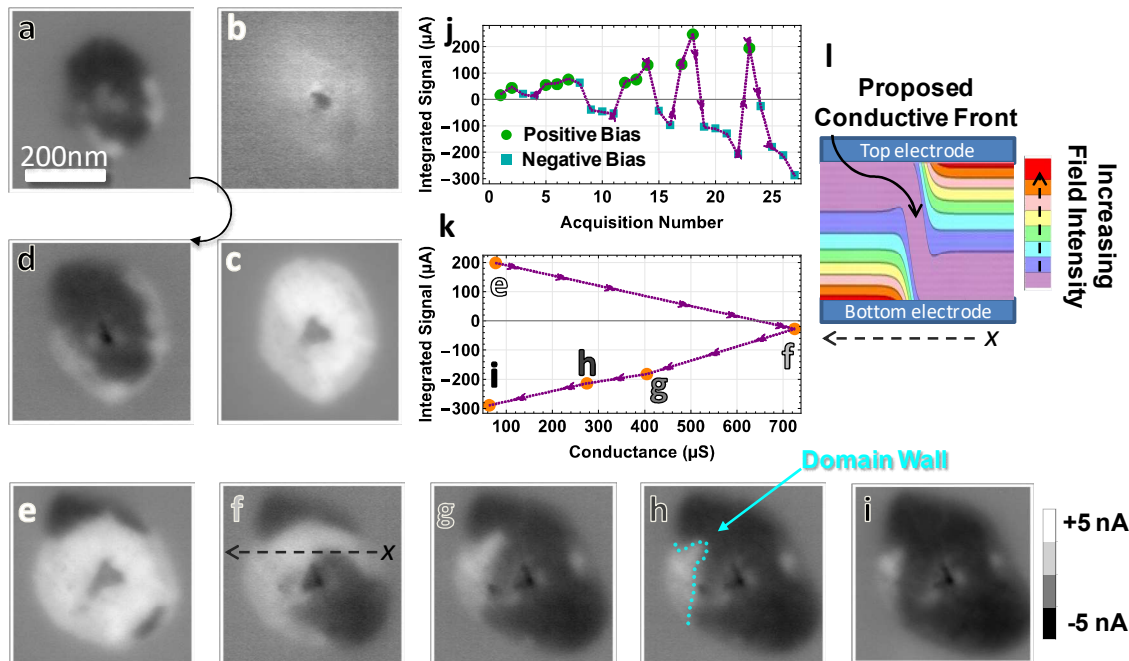


Figure 7. a-d) 5 keV EBIC images of alternating hard changes in polarization observed in symmetric devices. The sign of the measured current is changing since the device built in field is changing direction as a consequence of programming. e-i) Gradual movement of a domain wall around a barrier to encompass the entire switching region. j) Plot of effect of programming bias on device polarization with increasing amplitude of bias. k) Relationship between total EBIC signal and conductance (at 0.1 V) from stepwise transition from e to i. l) Cartoon depiction of the polarization domains with a reversal in field concentration from the top electrode to the bottom electrode with distance.

References

- [1] J. J. Yang, *et al.*, "Memristive devices for computing," *Nature Nanotechnol.*, vol. 8, pp. 13-24, 2013.
- [2] J. J. Yang, *et al.*, "High switching endurance in TaO_x memristive devices," *Applied Physics Letters*, vol. 97, p. 232102, 2010.
- [3] B. Govoreanu, *et al.*, "10x10nm Hf/HfO_x crossbar resistive RAM with excellent performance, reliability and low-energy operation," in *Electron Devices Meeting (IEDM), 2011 IEEE International*, 2011, pp. 31.6.1-31.6.4.
- [4] S. Kim, *et al.*, "Comprehensive Physical Model of Dynamic Resistive Switching in an Oxide Memristor," *ACS Nano*, vol. 8, pp. 2369-2376, 2014/03/25 2014.
- [5] D. B. Strukov, *et al.*, "Coupled Ionic and Electronic Transport Model of Thin-Film Semiconductor Memristive Behavior," *Small*, vol. 5, pp. 1058-1063, 2009.
- [6] S. Menzel, *et al.*, "Origin of the Ultra-nonlinear Switching Kinetics in Oxide-Based Resistive Switches," *Advanced Functional Materials*, vol. 21, pp. 4487-4492, 2011.
- [7] D. B. Strukov, *et al.*, "Thermophoresis/diffusion as a plausible mechanism for unipolar resistive switching in metal-oxide-metal memristors," *Applied Physics A*, vol. 107, pp. 509-518, 2012.
- [8] Y. Yang, *et al.*, "Oxide Heterostructure Resistive Memory," *Nano Letters*, vol. 13, pp. 2908-2915, 2013/06/12 2013.
- [9] J. Kwon, *et al.*, "Transient Thermometry and High-Resolution Transmission Electron Microscopy Analysis of Filamentary Resistive Switches," *ACS Applied Materials & Interfaces*, vol. 8, pp. 20176-20184, 2016/08/10 2016.
- [10] J. P. Strachan, *et al.*, "Spectromicroscopy of tantalum oxide memristors," *Applied Physics Letters*, vol. 98, p. 242114, 2011.
- [11] S. Kumar, *et al.*, "Direct Observation of Localized Radial Oxygen Migration in Functioning Tantalum Oxide Memristors," *Advanced Materials*, vol. 28, pp. 2772-2776, 2016.
- [12] J. J. Yang, *et al.*, "The mechanism of electroforming of metal oxide memristive switches," *Nanotechnology*, vol. 20, p. 215201, 2009.
- [13] U. Celano, *et al.*, "Imaging the Three-Dimensional Conductive Channel in Filamentary-Based Oxide Resistive Switching Memory," *Nano Letters*, vol. 15, pp. 7970-7975, 2015/12/09 2015.
- [14] D. E. Ioannou and C. A. Dimitriadis, "A SEM-EBIC minority-carrier diffusion-length measurement technique," *IEEE Transactions on Electron Devices*, vol. 29, pp. 445-450, 1982.
- [15] H. P. Yoon, *et al.*, "Local electrical characterization of cadmium telluride solar cells using low-energy electron beam," *Solar Energy Materials and Solar Cells*, vol. 117, pp. 499-504, 2013.
- [16] P. M. Haney, *et al.*, "Electron beam induced current in the high injection regime," *Nanotechnology*, vol. 26, p. 295401, 2015.
- [17] M. Kittler and W. Seifert, "On the origin of EBIC defect contrast in silicon. A reflection on injection and temperature dependent investigations," *physica status solidi (a)*, vol. 138, pp. 687-693, 1993.
- [18] S. Hanke, *et al.*, "Computer simulation of internal electron emission in ion-bombarded metals," *Nuclear Instruments and Methods in Physics Research*

- Section B: Beam Interactions with Materials and Atoms*, vol. 303, pp. 55-58, 2013.
- [19] S. Hanke, *et al.*, "A hybrid model describing ion induced kinetic electron emission," *Nuclear Instruments and Methods in Physics Research Section B: Beam Interactions with Materials and Atoms*, vol. 352, pp. 18-21, 2015.
- [20] P. Lin and H. Leamy, "Tunneling current microscopy," *Applied Physics Letters*, vol. 42, pp. 717-719, 1983.
- [21] J. Goldstein, *et al.*, *Scanning Electron Microscopy and X-Ray Microanalysis: A Text for Biologists, Materials Scientists, and Geologists*: Springer US, 2013.
- [22] P. Hovington, *et al.*, "CASINO: A new Monte Carlo code in C language for electron beam interactions—part III: Stopping power at low energies," *Scanning*, vol. 19, pp. 29-35, 1997.
- [23] D. Drouin, *et al.*, "CASINO: A new monte carlo code in C language for electron beam interactions—part II: Tabulated values of the mott cross section," *Scanning*, vol. 19, pp. 20-28, 1997.
- [24] D. Drouin, *et al.*, "CASINO V2.42—A Fast and Easy-to-use Modeling Tool for Scanning Electron Microscopy and Microanalysis Users," *Scanning*, vol. 29, pp. 92-101, 2007.
- [25] C. Rossel, *et al.*, "Electrical current distribution across a metal–insulator–metal structure during bistable switching," *Journal of Applied Physics*, vol. 90, p. 2892, 2001.
- [26] L. Yi Meng, *et al.*, "Elimination of high transient currents and electrode damage during electroformation of TiO₂ -based resistive switching devices," *Journal of Physics D: Applied Physics*, vol. 45, p. 395101, 2012.
- [27] T. E. Madey and J. T. Y. Jr., "Electron-Stimulated Desorption as a Tool for Studies of Chemisorption: A Review," *Journal of Vacuum Science and Technology*, vol. 8, pp. 525-555, 1971.
- [28] D. J. Smith, *et al.*, "The electron-beam-induced reduction of transition metal oxide surfaces to metallic lower oxides," *Ultramicroscopy*, vol. 23, pp. 299-303, 1987.
- [29] P. Hovington, *et al.*, "CASINO: A new Monte Carlo code in C language for electron beam interaction—Part I: Description of the program," *Scanning*, vol. 19, pp. 1-14, 1997.
- [30] G. F. Dionne, "Origin of secondary-electron-emission yield-curve parameters," *Journal of Applied Physics*, vol. 46, p. 3347, 1975.
- [31] R. Alig and S. Bloom, "Electron-hole-pair creation energies in semiconductors," *Physical Review Letters*, vol. 35, p. 1522, 1975.
- [32] I. A. Glavatskikh, *et al.*, "Self-consistent electrical charging of insulating layers and metal-insulator-semiconductor structures," *Journal of Applied Physics*, vol. 89, p. 440, 2001.
- [33] P. M. Haney, *et al.*, "Depletion region surface effects in electron beam induced current measurements," *Journal of Applied Physics*, vol. 120, p. 095702, 2016.
- [34] P. R. Mickel, *et al.*, "A physical model of switching dynamics in tantalum oxide memristive devices," *Applied Physics Letters*, vol. 102, p. 223502, 2013.
- [35] P. R. Mickel, *et al.*, "Power signatures and vacancy profile control in nanoscale memristive filaments," *Applied Physics Letters*, vol. 107, p. 033507, 2015.

- [36] P. R. Mickel, *et al.*, "Isothermal Switching and Detailed Filament Evolution in Memristive Systems," *Advanced Materials*, vol. 26, pp. 4486-4490, 2014.
- [37] S. M. Sze and K. K. Ng, *Physics of semiconductor devices*: John wiley & sons, 2006.
- [38] F. Miao, *et al.*, "Continuous electrical tuning of the chemical composition of TaO_x-based memristors," *ACS Nano*, vol. 6, pp. 2312-2318, 2012.
- [39] Y. M. Lu, *et al.*, "Impact of Joule heating on the microstructure of nanoscale TiO₂ resistive switching devices," *Journal of Applied Physics*, vol. 113, p. 163703, 2013.
- [40] J. J. Yang, *et al.*, "A family of electronically reconfigurable nanodevices," *Advanced Materials*, vol. 21, pp. 3754-3758, 2009.
- [41] A. Marchewka, *et al.*, "Physical simulation of dynamic resistive switching in metal oxides using a Schottky contact barrier model," in *2015 International Conference on Simulation of Semiconductor Processes and Devices (SISPAD)*, 2015, pp. 297-300.
- [42] A. Schonhals, *et al.*, "Critical ReRAM Stack Parameters Controlling Complimentary versus Bipolar Resistive Switching," in *2015 IEEE International Memory Workshop (IMW)*, 2015, pp. 1-4.